AN ABSTRACT OF THE THESIS OF

Stéphanie Melin for the degree of Master of Science in Chemistry presented on September 4, 2002.

Title: APPLICATIONS OF NONLINEAR RAMAN SPECTROSCOPY

Redacted for Privacy

Abstract approved: Joseph W. Nibler

Two nonlinear optical experiments are presented in which the third-order electronic susceptibility of molecules is used to generate Raman signals. The first one uses a single 532 nm beam from a Nd:YAG laser to produce Stimulated Raman Scattering in benzene and deuterated benzene. With a simple experimental set-up, stimulated emission involving CC and CH (CD) stretching modes from both C_6H_6 and C_6D_6 can be visually witnessed. Collinear and conical stimulated Raman beams are observed and explained. Measuring the wavelengths of the coherent beams with a meter stick and a grating permits the calculation of CC and CH force constants in benzene. This experiment has been developed as a lab in graduate and undergraduate courses and has been submitted to J. Chem. Ed. for publication.

The second experiment uses a high resolution Coherent Anti-Stokes spectrometer to investigate the ν_1 vibrational mode of the CD_3 radical produced by photolysis of CD_3I. Calibrated spectra are obtained at much higher resolution than

in an earlier published study and efforts are described to improve the range of data and to reconcile differences between the spectra. Modeling of the spectra leads to a "best fit" set of vibration-rotation parameters for CD_3 but a completely satisfactory fit of both high and low resolution spectra was not achieved.

APPLICATIONS OF NONLINEAR RAMAN SPECTROSCOPY

by

Stéphanie Melin

A THESIS

submitted to

Oregon State University

in partial fulfillment of
the requirements for the
degree of

Master of Science

Presented September 4, 2002
Commencement June 2003

Master of Science thesis of Stéphanie Melin presented on September 4, 2002.

APPROVED:

Redacted for Privacy

Major Professor, representing Chemistry

Redacted for Privacy

Head of the Department of Chemistry

Redacted for Privacy

Dean of the Graduate School

I understand that my thesis will become part of the permanent collection of Oregon State University libraries. My signature below authorizes release of my thesis to any reader upon request.

Redacted for Privacy

Stéphanie Melin, Author

ACKNOWLEDGMENTS

First, I need to thank my parents and my brother for believing in me more than I even do and encouraging me to realize one of my dreams: studying in the United States. I also have to thank my family for just being there and eager to see me even for a short time whenever I would go home. I just wished Papi Corbie could witness this accomplishment.

I must also thank Dr Nibler, Joe, for being a wonderful advisor. His way of thinking and resolving problems amazes me every single time. Thank you as well for letting me go home when I needed to. I will not be able to forget the water-ski trips, part of the group's requirements for graduation...

I need to thank as well our research group. Nicu, who made me think twice to what chemistry I should get involved in; thank you Nicu. Engelene, for being my friend, for making me laugh so much. Tony, for teaching me so much about this lab and the huge help you provided me in order to get some data. Jeff, for making me more French than I ever thought I would be. Dr Kyong Hee Lee, for the wonderful conversations in our office.

I wish to thank Intel for the financial support concerning the Benzene Experiment and the Chemistry Department for the support during my stay here and for giving me the opportunity to see how good, or how bad, of a teacher I could be.

I do not forget all my friends back home: Sophie (Doudou) with who I am going to get so much talking, dancing and partying back; Mélanie, my life-long

friend; Manue and Laurent as well as Karine and Florence for waiting for me; the "musicians" for giving me this little joy that is music to me; and all the friends from Mechanical Engineering.

There is one more person I need to thank, as well as his family. Arjan, my boyfriend, who is going through this process with me. Your personality helped me so much. The way you handle my stressful times is remarkable. Thank you for getting the best out of me, thank you for loving me.

TABLE OF CONTENTS

TABLE OF CONTENTS (Continued)

LIST OF FIGURES

LIST OF FIGURES (Continued)

LIST OF TABLES

LIST OF APPENDIX TABLES

APPLICATIONS OF NONLINEAR RAMAN SPECTROSCOPY

CHAPTER 1

INTRODUCTION

1.1 – HISTORY OF LINEAR RAMAN SPECTROSCOPY

In 1928, while returning to India from a visit to Oxford University, Sir Chandrasekhra Venkata Raman, the physicist, was struck by the intense blue color of the Mediterranean Sea. According to J. Rayleigh's explanation of the day, this color was due to the refraction of light. Raman proved that this was not correct, although he did include Rayleigh's idea that the process involved molecules and the scattering of light[1]. By studying the scattering of light in liquids with only the filtered sunlight as the source, a telescope as a collector, a complementary filter, and his eyes as the detector[2], Raman experimentally observed new radiation shifted to the red in wavelength. This was later explained, thanks to the quantum theory, as a property of molecular vibrations in the scattering medium. This effect was subsequently called the Raman effect in his honor.

By the end of the 1930s, Raman spectroscopy was an important method of non-destructive chemical analysis. Subsequently, as infrared spectroscopy

improved significantly during the following decades, Raman spectroscopy was displaced. However with the development of lasers in the 1960s, and sensitive multi-channel detectors later, Raman spectroscopy has become an important scientific and analytical tool. It is now widely used in laboratories all around the world. In addition, new nonlinear forms of Raman scattering have been developed, as discussed below.

1.2 – NONLINEAR SCATTERING OF LIGHT

When monochromatic light is projected on a sample, part of it can be shifted to a lower frequency (Stokes lines) from the incident frequency. This is due to the molecules of the sample being excited by the light. This process, called the Spontaneous Raman Effect (Figure 1-1) is very weak; out of a million photons, only ca. one will be at a shifted frequency[3]. In this case, the electric polarization of the sample is found to be linearly dependent on the strength of the electric field of the light[4].

$$P(t) = \chi^{(1)}E(t) \qquad 1\text{-}1$$

where P is the polarization (induced dipole per volume), and E is the electrical field. $\chi^{(1)}$ represents the linear susceptibility (polarizibility) of the medium.

The electric field strength can be expressed as

$$E(t) = E_0 \cos(\omega_0 t) \qquad 1\text{-}2$$

where E_0 is the amplitude of the wave and ω_0 is the frequency in radians.

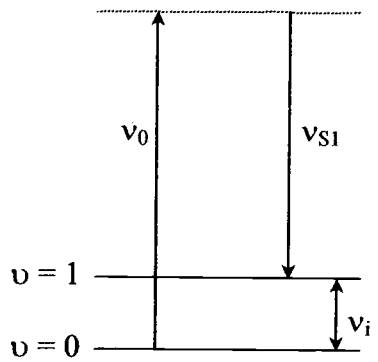

Figure 1-1 – Energy level diagram for the Spontaneous Raman Effect

When the intensity of the incident light increases to very high values, the polarization P requires nonlinear terms:

$$P(t) = \chi^{(1)}E(t) + \chi^{(2)}E^2(t) + \chi^{(3)}E^3(t) + \ldots \qquad 1\text{-}3$$

and these higher terms can produce new frequency components. For example, consider the second term:

$$P^{(2)}(t) = \chi^{(2)}\, E^2(t) \qquad 1\text{-}4$$

Substituting equation 1-2 in equation 1-4, we obtain

$$P^{(2)}(t) = \chi^{(2)}\; E_0^2 \cos^2(\omega_0 t) = \frac{\chi^{(2)}}{2} E_0^2\,[1 + \cos(2\omega_0 t)] \qquad 1\text{-}5$$

Therefore, if the second-order coefficient $\chi^{(2)}$ is non-zero, with a sufficient electrical field, the polarization acts as a source of new radiation scattered at a frequency equal to twice the original one. This "Doubling Process" is called Second-Harmonic Generation (Figure 1-2).

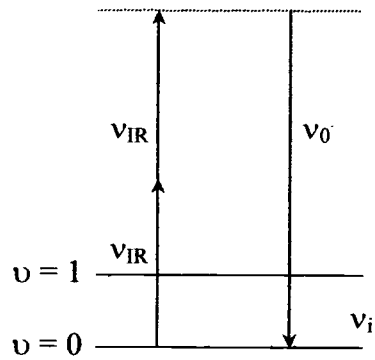

Figure 1-2 – Energy level diagram for the Doubling Process

In one important application, this process is used to create a green beam at 532 nm from an infrared one at 1064 nm produced by Nd:YAG lasers. Typically this doubling is done in a crystal like KDP (Potassium Dihydrogen Phosphate); which must be oriented at an angle such that phase matching (momentum conservation) is achieved. By doubling again this green beam with another KDP crystal at a different angle, one can generate ultraviolet radiation at 266 nm.

It is worth pointing out that equation 1-5 can also be written with two different frequencies:

$$P^{(2)}(t) = \chi^{(2)}\ E_0^{'} \cos(\omega_1 t)\ E_0^{''} \cos(\omega_2 t) \qquad 1\text{-}6$$

Using trigonometric relations, one can get

$$P^{(2)}(t) = \frac{\chi^{(2)}}{2}\ E_0^{'}\ E_0^{''}\ \{\cos[(\omega_1 + \omega_2)t]\ + \cos[(\omega_1 - \omega_2)t]\} \qquad 1\text{-}7$$

These terms correspond to Sum-Frequency Generation ($\omega_1 + \omega_2$) and Difference-Frequency Generation ($\omega_1 - \omega_2$), respectively.

This thesis will focus on the third term of equation 1-3, the third-order susceptibility. Two different processes will be introduced, discussed and applied for experiments done in this thesis. These are:

(Chapter 2) Stimulated Raman spectroscopy of benzene and its fully deuterated form (Chapter 3) Coherent Anti-Stokes Raman Scattering spectroscopy of CD_3 radical.

The former describes the development of a new experiment now used in three courses at OSU; Chem 464 Integrated Lab; Chem 567 Molecular Spectroscopy; Chem 681 Nonlinear Optical Interactions in Materials. This experiment has also been submitted for publication in the Journal of Chemical Education.

CHAPTER 2

STIMULATED RAMAN SCATTERING OF BENZENE

2.1 - INTRODUCTION

Because of the decreasing cost of pulsed lasers, new laser-based experiments are available to undergraduate students, broadening their knowledge of today's technology, and hence improving their access to the job market. In this chapter a new laboratory experiment is described which is particularly attractive to students because of visual effects and simplicity of data acquisition. This experiment involves the generation of intense nonlinear Raman radiation. A laser beam is focused in a medium with a strong Raman transition ν_{vib}, generating new frequency components. By measuring these frequencies with a simple meter stick, frequencies of vibration and force constants of the molecule can be determined. The medium chosen was benzene, since it generates spectacular new colored "laser" beams and the spectrum of these is readily interpreted.

2.2 – THEORY OF STIMULATED RAMAN SCATTERING

By considering the third term of equation 1-3, and using the same analogy as for the second order susceptibility, one can see that many other frequencies can be created via the $\chi^{(3)}$ term. This chapter will focus on one of the light generation processes: Stimulated Raman Scattering, which can have a conversion efficiency of >10%.

In this process, three waves are focused on a sample with a molecular resonance ν_i to create a fourth wave. For example, three incident beams might involve two fundamentals at frequency ν_0, along with a weak frequency shifted beam (ν_{S1}) as in Figure 2-1. The output beam is also at the first Stokes frequency $\nu_{S1} = 2\nu_0 - \nu_{S1} - 2\nu_i = \nu_0 - \nu_i$.

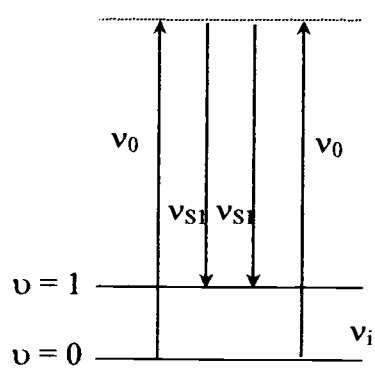

Figure 2-1 – Energy level diagram for the Stimulated Raman Scattering

For this case, the polarization P becomes:

$$P(\nu_1) = \chi^{(3)} E(\nu_0)\, E(\nu_0)\, E(\nu_{S1}) \qquad 2\text{-}1$$

and this causes the intensity $I(\nu_{S1})$ of $E(\nu_{S1})$ to grow exponentially[5] with the distance z:

$$I(\nu_{S1}) = I_0(\nu_{S1}) \exp(zG) = I_0(\nu_{S1}) \exp\left[\frac{zKN \dfrac{d\sigma}{d\nu_S} I(\nu_0)}{\Delta\nu_S}\right] \qquad 2\text{-}2$$

Here G is the gain coefficient, K a proportionality constant, N the number density, $d\sigma/d\nu_S$ the Raman scattering spectral cross-section and $\Delta\nu_S$ the frequency width of the Raman transition. $I(\nu_0)$ is the intensity of the main pump beam and the initial Stokes intensity $I_0(\nu_{S1})$ corresponds to the weak intensity of a photon Raman scattered in the direction of propagation of the ν_0 laser beam. To have amplification of ν_{S1}, the intensity $I(\nu_0)$, must be high enough for the Raman gain to overcome absorption or scattering losses of $I(\nu_{S1})$. Then an intense coherent beam (S_1) is generated along the z-axis, in contrast to spontaneous Raman Spectroscopy, where the scattering is in all directions.

Similarly, if $I(\nu_{S1})$ is high enough, it can follow the same scheme and generate a new beam, the second Stokes output at $\nu_{S2} = \nu_{S1} - \nu_i$. This process can go on as long as the intensity of each new beam produced is high enough to generate another one. With benzene, four Stokes beams are visible. The wavelength of these generated beams can be measured to calculate the ν_i transition frequency.

2.3 – MOMENTUM AND ENERGY CONSERVATION

The momentum of a wave at frequency ν_j traveling through a material with index of refraction n_j is proportional to the wavevector magnitude $k_j = 2\pi n_j \nu_j / c$ (c is the velocity of light). The momentum matching conditions for Stimulated Raman Scattering is:

$$\mathbf{k}_{S1} = \mathbf{k}_0 - \mathbf{k}_i \qquad 2\text{-}3$$

Thus the momentum conservation corresponds to a collinear vector addition (Figure 2-2).

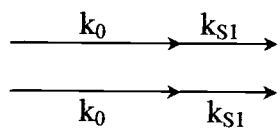

Figure 2-2 - Momentum conditions for SRS

In addition to this collinear process, a second process involving the third-order susceptibility occurs: Coherent Anti-Stokes Raman Scattering. It generates non-collinear beams at frequencies $\nu_{A1} = 2\nu_0 - \nu_{S1} = \nu_0 + \nu_i$ (Anti-Stokes) and $\nu_{S1} = \nu_0 - \nu_i$ (Stokes). Its energy level diagram and its momentum-matching condition are described in Figure 2-3. The theory will be explained in more detail later.

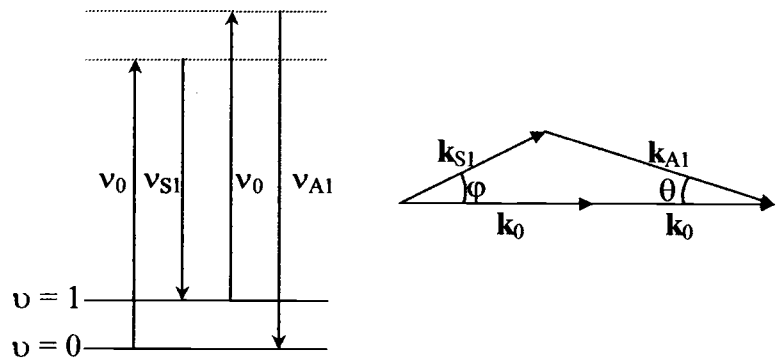

Figure 2-3 – Energy level diagram and momentum conservation for CARS

Thus, according to Figure 2-3, momentum conservation demands $2\mathbf{k}_0 = \mathbf{k}_{S1} + \mathbf{k}_{A1}$. Because of dispersion (variation of the index of refraction with wavelength), this implies that the Stokes and the Anti-Stokes beams are generated at a slight angle to the pump beam. For liquid benzene, this angle reaches 4° and as shown later, rings are clearly visible on the Anti-Stokes and Stokes side of the pump beam[5] (although the red Stokes ring is hard to distinguish from the collinear beam generated by the SRS process).

2.4 – EXPERIMENTAL SET-UP

Our experiment is similar to one described by Grant and Hardwick in 1997[6], where a monochromator and a CCD detector were used to measure the wavelengths

of the stimulated Raman beams. We too used such a spectrometer system for greater accuracy of wavelength results. However, we also show that a simple grating and a meter stick are sufficient for good results. Figure 2-4 shows an experimental set-up allowing both variants: measurements with a transmission grating as well as with a monochromator.

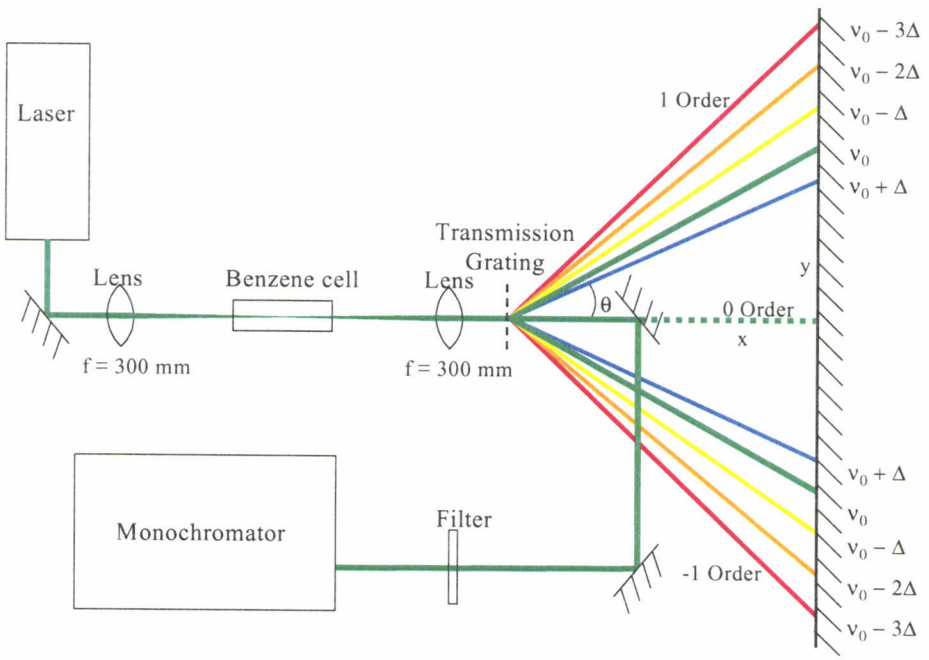

Figure 2-4 – Experimental set-up

The pump beam is produced by a Q-switched Nd:YAG laser (Quanta-Ray DCR/A or Molectron MY34) with second harmonic generator capable of generating more

than 100 mJ 532 nm pulses of 5-10 ns duration. In fact, only 1-3 mJ of 10 ns pulse duration is required since this gives a peak power of 100 kW and intense SRS beams. The beam is focused with a 300-mm focal length lens in the center of a 290-mm long, 9-mm diameter cell made of two O-ring joints sealed together. Each opening of the cell is sealed with Viton O-rings and windows, the whole cell being held together with metal ball joint clamps. (Because of its high carcinogenicity[7], the benzene must be poured into the cell in a hood). A transmission grating disperses the different generated beams for the further measurements. The second lens serves to focus the emerging beam onto a perpendicular screen. Figure 2-5 shows a result of this focusing on the blue Anti-Stokes ring produced in benzene.

Figure 2-5 – Blue Anti-Stokes ring

2.5 – RESULTS

Figure 2-6 shows an actual picture of what the eye sees when the beams are dispersed on a wall. It is assumed that only the symmetric CC and CH stretches are involved in this experiment.

Figure 2-6 – Digital picture of dispersed beams with their assignments for (a) C_6H_6, (b) C_6D_6

The wavelength of each beam is obtained by measuring the distance y_i of each spot to the zero-order beam and the distance x of the wall to the grating. Using equation

2-4, the angle of diffraction is obtained and used in the transmission grating equation (2-5) for an angle of incidence equal to zero[8].

$$\tan \theta_i = y_i/x \qquad 2\text{-}4$$

$$n\lambda_i = d \sin \theta_i \qquad 2\text{-}5$$

Table 2-1 shows some typical measurements performed following this method with a grating of 833 grooves/mm and a distance from the wall equal to y = 33 cm.

x (cm)	θ (rad)	λ (nm)	ν (cm^{-1})	n	m
25.5	0.658	509.34	19633.4	1	0
27.75	0.699	536.12	18652.6	0	0
30.5	0.746	565.39	17686.8	-1	0
34.1	0.802	598.60	16705.8	-2	0
38.8	0.866	634.53	15759.6	-3	0
39.5	0.875	639.26	15643.0	0	-1
46.85	0.957	681.02	14683.9	-1	-1
45.7	0.945	675.33	14807.5	-1	-1
38.55	0.863	632.81	15802.6	0	-1
37.95	0.855	628.59	15908.7	-3	0
33.35	0.791	592.12	16888.5	-2	0
29.9	0.736	559.31	17879.1	-1	0
27.2	0.689	529.82	18874.4	0	0
25.05	0.649	503.65	19855	1	0

Table 2-1 – Distance/frequency measurements of C_6H_6

The coefficients n and m are used to fit the frequencies in equation 2-6 through a linear regression.

$$\nu_n = \nu_0 + n\,\nu_{CC} + m\,\nu_{CH} \qquad 2\text{-}6$$

Table 2-2 gathers typical results from such an experiment as well as the ones obtained using a monochromator.

Molecule		Literature values[9]	Monochromator measurements	Wall measurements
C_6H_6	ν_{CC}	991.6	991 ± 2	990 ± 10
	ν_{CH}	3061.9	3062 ± 6	3100 ± 30
C_6D_6	ν_{CC}	944.7	943 ± 2	950 ±10
	ν_{CD}	2292.3	2293 ± 6	2300 ± 30

Table 2-2 – Typical frequencies (cm^{-1}) results

One interesting feature of the measurements is the lineshapes of some of the Stokes and Anti-Stokes beams, which are displayed in Figure 2-7. It may be noted that the Anti-Stokes beams generated by the noncollinear process are significantly broadened compared to the collinear Stokes beam. This has been observed by

others and is explained in Ref. 5 as follows. Benzene is a Kerr liquid made of anisotropic molecules. Because these molecules are also nonpolar, they are randomly oriented. Once an optical field is applied, the molecules reorient themselves along the direction of the optical field. This is known as the Kerr effect. Because of the high viscosity of a liquid (in comparison with a gas), the molecules need energy to reorient; this can only be accomplished by a red-shifted photon scattering process: a transfer of energy between the optical field and the scattering molecule[5].

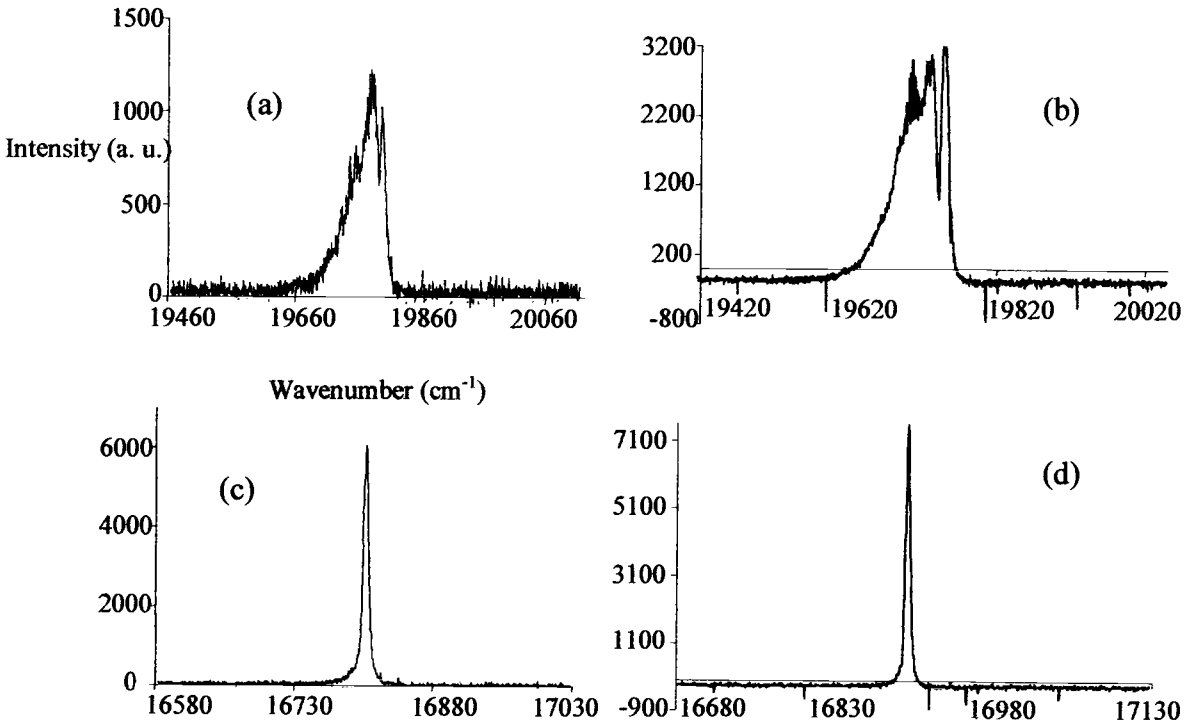

Figure 2-7 – Graphs of the Anti-Stokes (top) and second Stokes (bottom) for C_6H_6 (a) and (c), and C_6D_6 (b) and (d) respectively.

2.6 – FORCE CONSTANTS

The measurements give frequencies of two types of vibrations in benzene and permit the calculation of CH and CC force constants. The motions correspond to the two polarized a_{1g} vibrations. The appropriate coordinates of this symmetry are

$$S_1 = (s_1 + s_2 + s_3 + s_4 + s_5 + s_6)/(6)^{1/2} \qquad 2\text{-}7$$

$$S_2 = (t_1 + t_2 + t_3 + t_4 + t_5 + t_6)/(6)^{1/2} \qquad 2\text{-}8$$

where s_i and t_i are bond extensions of one of the six CH bonds and CC bonds respectively. These two a_{1g} coordinates contribute to the potential energy of the molecules:

$$U(A_{1g}) = \tfrac{1}{2}\, k_s S_1^2 + \tfrac{1}{2}\, k_t S_2^2 + k_{st} S_1 S_2 \qquad 2\text{-}9$$

The force constants are related to the vibrational frequencies and atomic masses through the relations

$$4\pi^2 \nu_1^2 + 4\pi^2 \nu_2^2 = k_s[(1/m_H) + (1/m_C)] - 2k_{st}/m_C + k_t/m_C \qquad 2\text{-}10$$

$$(4\pi^2 \nu_1^2)(4\pi^2 \nu_2^2) = (k_s k_t - k_{st}^2)/m_H m_C \qquad 2\text{-}11$$

Since, ν_1 and ν_2 (respectively ν_{CH} and ν_{CC}) are obtained for both isotopomers, it is thus possible to solve[10] for k_s, k_t and k_{st}. Figure 2-8 shows a display of the possible solutions for each isotopomer.

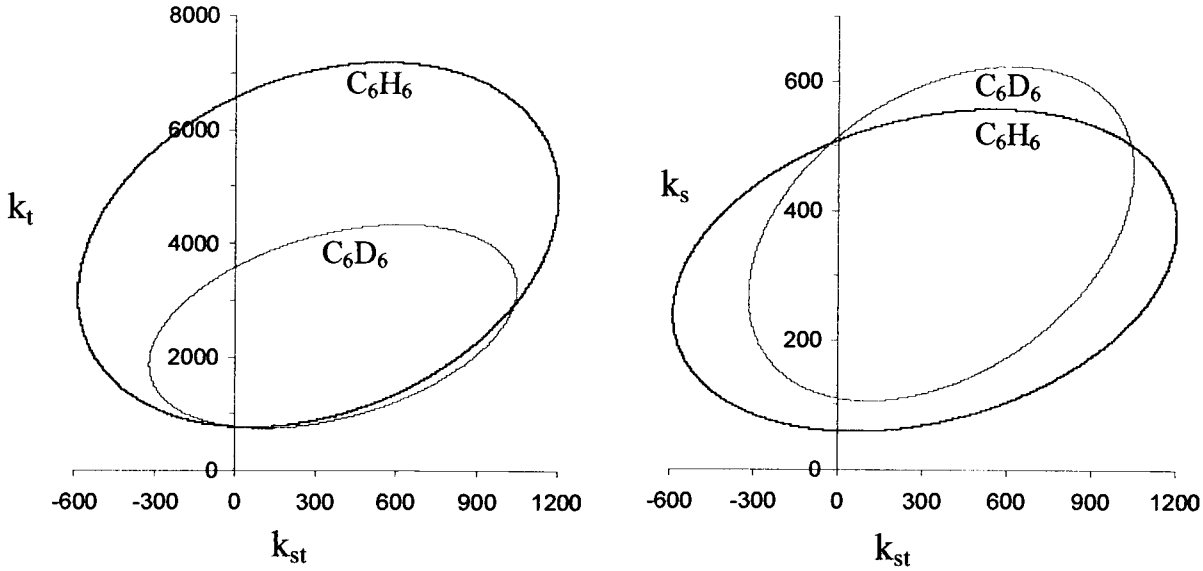

Figure 2-8 – Force constants displays for a_{1g} benzene vibrations

For each graph, two solutions are available (common intersection points). However only the one with the smallest k_{st} value is considered physically reasonable. In laboratory experiments, we use the Solver function of Excel to vary the force constants to minimize the sum of $(\nu_{iobs} - \nu_{icalc})^2$. Accurate results (Table 2-2) are obtained as well as their uncertainties derived from our estimate of the frequency uncertainties. These results can be compared to typical C-C, C=C, C≡C, C-H force constants values displayed in Table 2-3.

Force constants	Literature[10] values	Monochromator measurements	Wall measurements
k_s	504	503 ± 4	525 ± 20
k_t	776	775 ± 9	760 ± 40
k_{st}	-28	-30 ± 16	20 ± 80

Table 2-3 – Force constants (N/m) results using Solver in Excel

Bond	Force constants	
	CC stretch	CH stretch
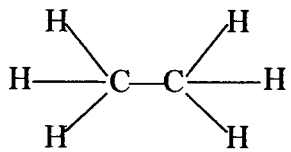	450	479
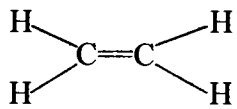	960	510
H—C≡C—H	1559	585

Table 2-4 – Typical CC and CH stretching force constants[9] in N/m

2.7 – CONCLUSION

A stimulated Raman experiment has been improved and simplified so that it is accessible to students. The experiment has been performed on liquid benzene. The ν_{CC}, ν_{CH}, and ν_{CD} frequency stretches were found in good agreement with the literature values. In addition, the different force constants were calculated using the displays of k_s versus k_{st} and k_t versus k_{st}.

CHAPTER 3

COHERENT ANTI-STOKES RAMAN SCATTERING OF CD_3

3.1 – INTRODUCTION

This chapter describes in more detail the CARS process and presents a study of the Raman active ν_1 symmetric CD stretching band of CD_3 radical, formed by UV photolysis of CD_3I. An earlier study on this species formed by photolysis of azomethane-d_6 was performed by Miller *et al.*[11] in 1989 at a resolution of 0.5 cm^{-1}; their experimental spectrum and calculated spectrum are reproduced in Figure 3-1.

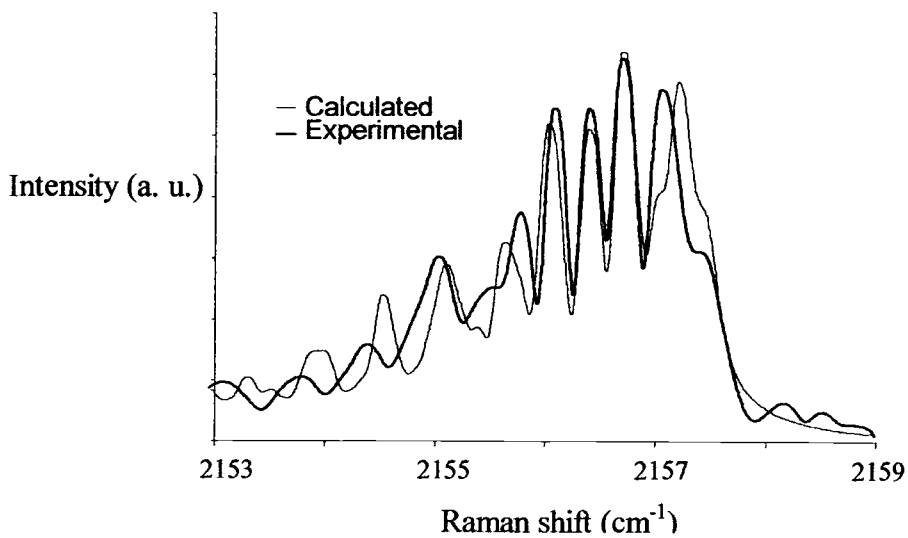

Figure 3-1 – CD_3 radical CARS experimental and calculated spectra from reference 11.

It is seen that the agreement between calculated and observed spectra is less than perfect, in part due to the limited resolution they had. Our lab equipment provides a spectral resolution of 0.001 cm^{-1}, and it was thought that this might give improved spectra, perhaps of the quality obtained in earlier studies of CH_3 in our lab[12].

In fact, during the research on the radical[12] CH_3, our group obtained some preliminary spectra of CD_3. Figure 3-2 shows a composite of these spectra as well as a CD_3I spectrum. Although our CD_3 spectra were not carefully calibrated, in comparing Figures 3-1 and 3-2 it can be seen that they bear little resemblance to those of Miller *et al.*, the band origin at high wavenumbers being apparently shifted by about 1 cm^{-1} and the rotational structure being quite different in the two cases. It was the purpose of this study to try to resolve these differences by carefully calibrating our spectra and by exploring ways to change the relative rotational populations to determine if the differences in the latter could explain the spectral differences. The overall objective is to obtain accurate vibrational-rotational parameters and force constants for methyl radical.

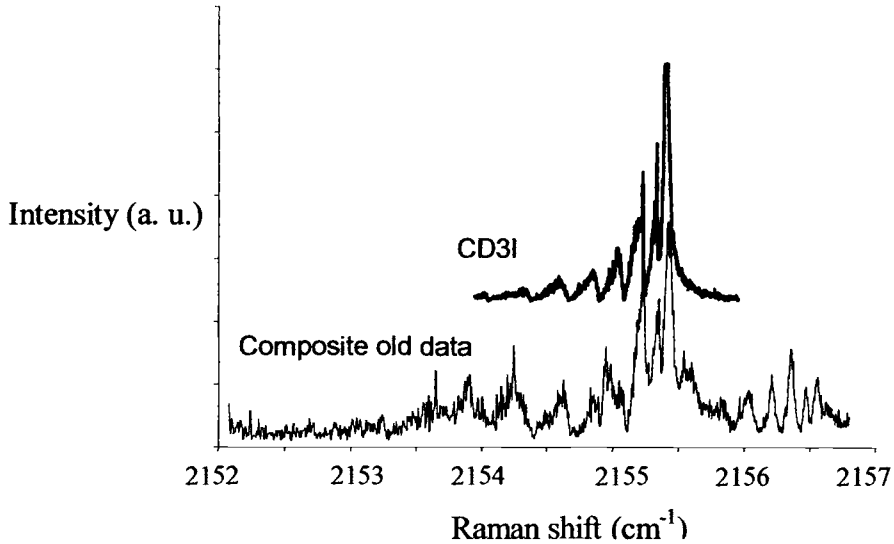

Figure 3-2 – Jet spectra of CD_3I and a composite of CD_3 data.

3.2 – THEORY OF COHERENT ANTI-STOKES RAMAN SCATTERING

In the previous chapter, the nonlinear interaction of a pump beam with a medium was shown to generate an anti-Stokes beam via a third-order $\chi^{(3)}$ term. This interaction can be caused to occur in a more controlled fashion by supplying, in addition to the pump beam, a tunable Stokes beam. This process, developed in this chapter, is called CARS spectroscopy, for Coherent Anti-Stokes Raman Scattering. It involves the generation of a coherent anti-Stokes photon from two pump photons and a first Stokes photon (Figure 3-3), leading to a signal of frequency $\nu_{A1} = 2\nu_0 - \nu_{S1} = \nu_0 + \nu_i$ (since $\nu_{S1} = \nu_0 - \nu_i$).

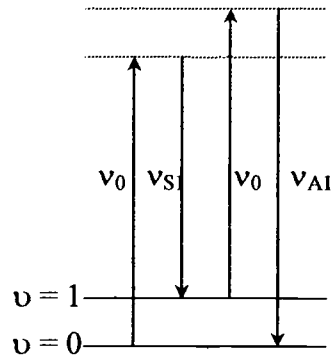

Figure 3-3 – Energy level diagram for CARS spectroscopy

For CARS spectroscopy, the sample is usually irradiated by beams propagating in a common collinear direction. CARS spectroscopy has several significant advantages over conventional Raman spectroscopy:

1. The anti-Stokes beam created is coherent and is emitted in one direction with a small solid angle so efficient collection of the signal is possible.
2. The frequency is to the blue of the pump beam, which prevents interference by fluorescence, which normally occurs to the red side (Stokes region).
3. The strength of the CARS signal can be a million times stronger than Raman signals, allowing a small concentration of gaseous compounds to be detected.
4. The measurement requires high intensity beams and is thus done with pulsed, focused lasers. This results in high temporal and spatial resolution.

5. The resolution is determined by the resolution of the lasers, not by a spectrometer. This results in an improvement of two or three orders of magnitude in spectral resolution.

The biggest disadvantages of CARS are the cost associated with the tunable laser and the fact that the sample has to be optically transparent and not easily damaged by the high power of the focused beams[13]. Thus it finds widest application in the study of gases.

The third-order susceptibility $\chi^{(3)}$ is the molecular parameter involved in CARS spectroscopy, which is a form of four-wave mixing. Knowing the polarization, the frequency, the phase and the magnitude of three input beams, one can evaluate these properties for the generated fourth anti-Stokes beam. Energy conservation requires that $\nu_{A1} = 2\nu_0 - \nu_{S1}$, while momentum conservation yields the phase-matching condition $\mathbf{k}_{A1} = 2\mathbf{k}_0 - \mathbf{k}_{S1}$; $k_j = 2\pi n_j \nu_j / c$ stands for the wave vector magnitude which is proportional to the momentum of the photon at frequency ν_j traveling through a material with index of refraction n_j. In one common form of the CARS experiment the incident beams are set up according to the so-called BOXCARS phase-matching diagram (Figure 3-4).

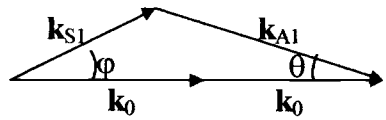

Figure 3-4 – CARS phase matching conditions

A collinear arrangement, which gives best overlap of the beams at a focus, is possible in gases but the noncollinear geometry shown above is often used since it has some significant advantages. First, it minimizes the generation from air, windows, lenses etc. of a background CARS signal caused by a nonresonant $\chi^{(3)}$ term that is present in these materials. This is because the beams only overlap at the focus. This overlap geometry also constitutes a second advantage in that it gives improved spatial resolution. Finally, the most important advantage comes from the angular separation of the anti-Stokes beam relative to the other beams[14], making it possible to eliminate contributions by these much more intense sources. The latter effect is achieved with greatest efficiency in the folded BOXCARS geometry shown in Figure 3-5 below.

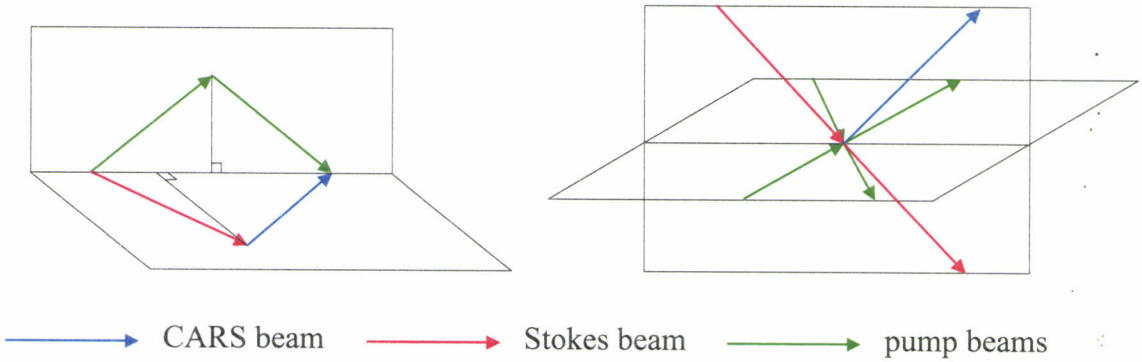

Figure 3-5 – Folded BOXCARS phase-matching diagrams and the actual incidence of the beams

As shown in reference 15 the intensity I_3 of the CARS beam is given by:

$$I_3 \propto \left|\chi^{(3)}_{CARS}\right|^2 I_1^2 I_2 \left[\frac{\sin\left(\frac{\Delta k \ell}{2}\right)}{\frac{\Delta k \ell}{2}}\right]^2 \qquad 3\text{-}1$$

with the phase mismatch given by $\Delta k = 2k_1 - k_2 - k_3$. Here k_1 is the wave vector of the pump beam, k_2 the wave vector of the Stokes beam, and k_3, the wave vector of the Anti-Stokes beam. I_1 and I_2 are the respective intensities of the pump and the Stokes beams, and ℓ is the interaction length. From this it can be seen that the intensity I_3 is a maximum when $\Delta k = 0$, meaning that the phase-matching conditions are optimal.

$\chi^{(3)}$, the third-order susceptibility, can be expressed as:

$$\chi^{(3)} \propto \frac{N_n - N_m}{\omega_{mn} - (\omega_1 - \omega_2) - i\Gamma_{mn}} \left(\frac{d\sigma}{d\Omega} \right) + \chi_{nr} \qquad 3\text{-}2$$

with N_n and N_m being the population density of the lower state and the upper state respectively, ω_{mn} being the frequency of the transition, Γ_{mn} being the damping constant of the transition, $\frac{d\sigma}{d\Omega}$ being the Raman cross-section of the molecule and χ_{nr} being the nonresonant term. Relations 3-1 and 3-2 are incorporated in the OSU program Specall, which was used in fitting CARS spectra obtained for CD_3 in this work.

3.3 – ABOUT THE RADICAL CD_3

CD_3 is an isotopomeric form of the methyl radical where D is a hydrogen atom with one neutron and one proton. The radical CH_3 is involved in combustion processes as a reactive species during the ignition and subsequent phases of burning[16]. It is a planar radical as has been proven through the years. CD_3 belongs to the D_{3h} point group, with one 3-fold axis, three 2-fold axis (along the C—D bonds), a plane of reflection perpendicular to the 3-fold axis, and three planes of reflection containing this axis and each of the C—D bonds. These different axes and planes are illustrated in Figure 3-6.

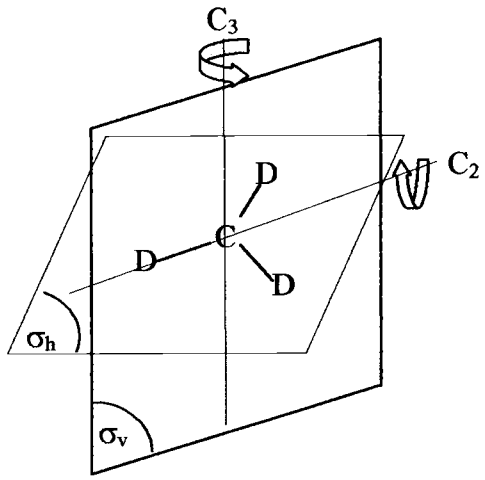

Figure 3-6 – Rotation axis and planes of reflection of the radical CD_3

The radical has four modes of vibration, illustrated in Figure 3-7. Two of them are degenerate, ν_3 and ν_4 which gives a total of six modes. ν_2, ν_3 and ν_4 are infrared active while ν_1, the symmetric stretch, can be seen only by Raman methods and hence is the mode of greatest interest in this work.

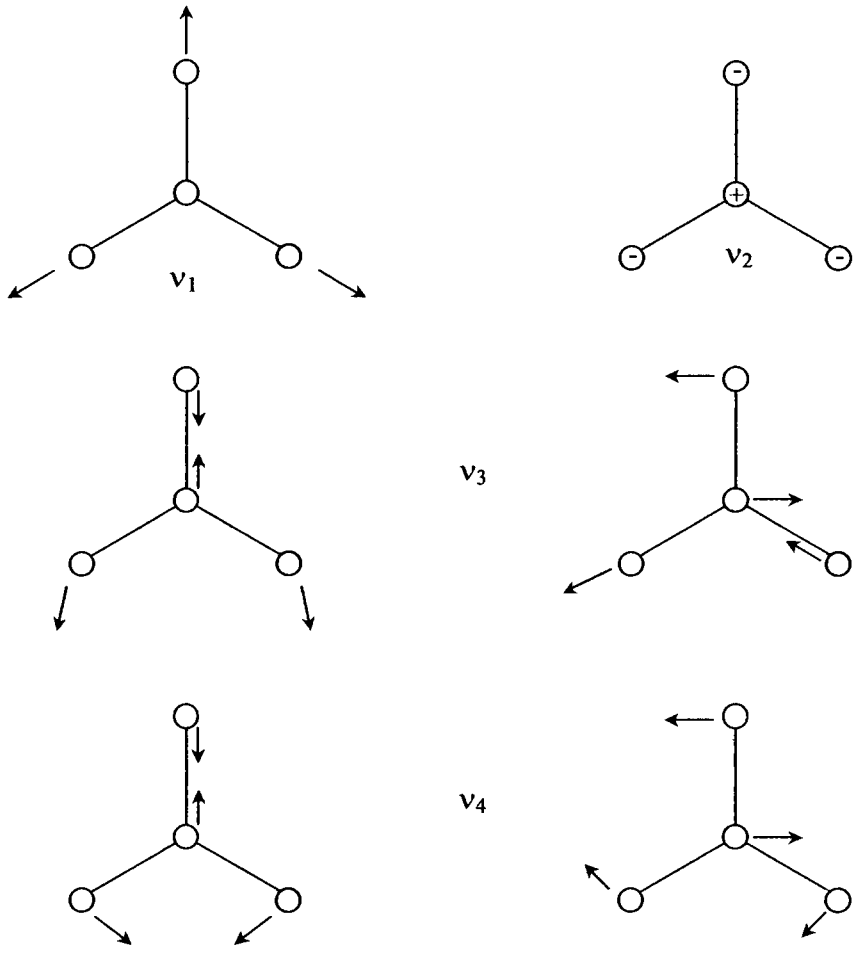

Figure 3-7 – Vibrational modes for CD_3 radical

3.4 – LITERATURE REVIEW OF WORK ON THE METHYL RADICAL

In 1956, G. Herzberg and J. Shoosmith[17] successfully investigated the CD_3 radical and its isotopomer CH_3 in vacuum UV using a flash photolysis technique to

produce the radicals. The UV bands were observed to be diffuse because of predissociation and showed Rydberg series. The work confirmed experimentally the prediction of a planar molecule from Walsh[18]. Herzberg later reported additional studies of the electronic structure[19] of the radical.

Throughout the years, especially in the last decades, many spectroscopic methods were used to study the ground electronic state properties of CH_3 and CD_3 radicals. Botschwina *et al.*[20] did *ab initio* calculations to determine the potential-energy surfaces and predict the ν_1 and ν_2 mode of CH_3 and CD_3 from UHF SCE wavefunctions. In one of the earliest experimental studies, Milligan *et al.*[21] photolysed CH_4 (and CD_4) in Ar and N_2 matrices to observe the CH_3 and CD_3 radicals using IR and UV detection. The ν_2 out of plane bending mode was seen at 611 cm^{-1} for $^{12}CH_3$ and 463 cm^{-1} for $^{12}CD_3$. Another method to produce the radicals was to photolyze the C—I bond in CH_3I and CD_3I molecules as done by Snelson[22] in 1970. The product radicals were then isolated in a cold matrix and examined by IR methods. The values of the ν_2, ν_3 and ν_4 were obtained for both isotopomers; since ν_1 is IR-inactive, it was not observed but it was estimated to be at 3044 cm^{-1} for CH_3 and 2153 cm^{-1} for CD_3. More than ten years later, additional structural properties of the ground electronic state were obtained using matrix isolation[23].

In the gas phase, a high resolution study of the ν_2 mode of CH_3 by diode laser of CH_3 by Yamada *et al.*[24] confirmed the planar geometry of the radical in its ground state. The $\nu_2 = 1\leftarrow0$, $2\leftarrow1$ and $3\leftarrow2$ bands were observed at 606.4531 cm^{-1},

681.6369 cm^{-1} and 731.0757 cm^{-1} respectively. The equilibrium bond length of C—H was observed to be 1.058 Å and the variation of the rotational constants of ν_2 with ν_2 quantum number were explained using the nonrigid invertor Hamiltonian and a model anharmonic potential energy function.

The ν_2 mode was studied further in the 80's for both CH_3 and CD_3 and some gas phase data were also obtained for $^{13}CH_3$, $^{13}CD_3$ and $^{13}CT_3$. From Van Veen *et al.*[25] to Sears *et al.*[26,27] and Parker *et al.*[28], many data are available: the values of the $\nu_2 = 1 \leftarrow 0$, $2 \leftarrow 1$ and $3 \leftarrow 2$ bands of CD_3 (457.8133 cm^{-1}, 507.9311 cm^{-1}, 542.4510 cm^{-1} respectively), the I^*/I ratio at 266 nm and accurate values for CH_3I and CD_3I bond energies are examples of reported results.

The ν_3 band was also seen in the gas phase. Starting in 1982 with Amano *et al.*[29], CH_3 was detected in absorption with a tunable difference frequency laser. The fundamental was found at 3160.8212 cm^{-1} and the vibration-rotation constants, $\alpha_3^B = 0.10679$ cm^{-1} and $\alpha_3^C = 0.04108$ cm^{-1}, were determined for the first time. Regarding CD_3, Sears *et al.*[30] observed the fundamental at 2391.08860 cm^{-1} and obtained as well its different molecular parameters; later on, using diode laser absorption spectroscopy, its transition moment[31] was measured at 0.030 ± 0.002 D. Another method of study used was the REMPI spectroscopy which yielded the ground state rotational constant[32] $B_0 = 4.798$ cm^{-1} for CD_3, and I^*/I branching ratio for various photolysis wavelengths[28,33].

The ν_4 mode has not yet been studied in the gas phase, presumably due to low intrinsic intensity. In a matrix, features at 1396 and 1026 cm^{-1} have been assigned for CH_3 and CD_3, respectively[22].

A high resolution CARS spectrum of the ν_1 mode was obtained by our group[12] of CH_3; the ν_1 transition appears at 3004.436 cm^{-1}. A resonance Raman spectroscopy study of CD_3 from Westre *et al.*[34] showed the presence of the ν_1 mode at 2155.0 cm^{-1}. The same year[11], a CARS experiment was performed on CD_3 radical and the ν_1 mode was reported at 2157.5 cm^{-1}.

Modes	CH_3	Ref	CD_3	Ref
Ground state	$B_0 = 9.57789$ cm^{-1} $C_0 = 4.74202$ cm^{-1}	24	$B_0 = 4.80198$ cm^{-1} $C_0 = 2.390$ cm^{-1}	26 20
ν_1	$\nu_0 = 3004.436$ cm^{-1} $B_1 = 9.48891$ cm^{-1} $C_1 = 4.6990$ cm^{-1}	12	$\nu_0 = 2157.5$ cm^{-1} $B_1 = 4.7759$ cm^{-1} $C_1 = 2.372$ cm^{-1}	11
ν_2	$1\leftarrow0$: 606.4531 cm^{-1} $2\leftarrow1$: 681.6369 cm^{-1} $3\leftarrow2$: 731.0757 cm^{-1} $B_2 = 9.25814$ cm^{-1} $C_2 = 4.811643$ cm^{-1}	24	$1\leftarrow0$: 457.8133 cm^{-1} $2\leftarrow1$: 507.9311 cm^{-1} $3\leftarrow2$: 542.4510 cm^{-1} $B_2 = 4.708648$ cm^{-1}	26
ν_3	$\nu_0 = 3160.8212$ cm^{-1} $B_3 = 9.47110$ cm^{-1} $C_3 = 4.70167$ cm^{-1}	29	$\nu_0 = 2381.08860$ cm^{-1} $B_3 = 4.758737$ cm^{-1} $C_3 = 2.373297$ cm^{-1}	30
ν_4	$\nu_0 = 1396$ cm^{-1}	22	$\nu_0 = 1026$ cm^{-1}	22

Table 3-1 – Summary of CH_3 and CD_3 vibrational frequencies and vibrational constants

3.5 - EXPERIMENTAL WORK

The CARS experimental apparatus shown below is described in detail in Ref. 35.

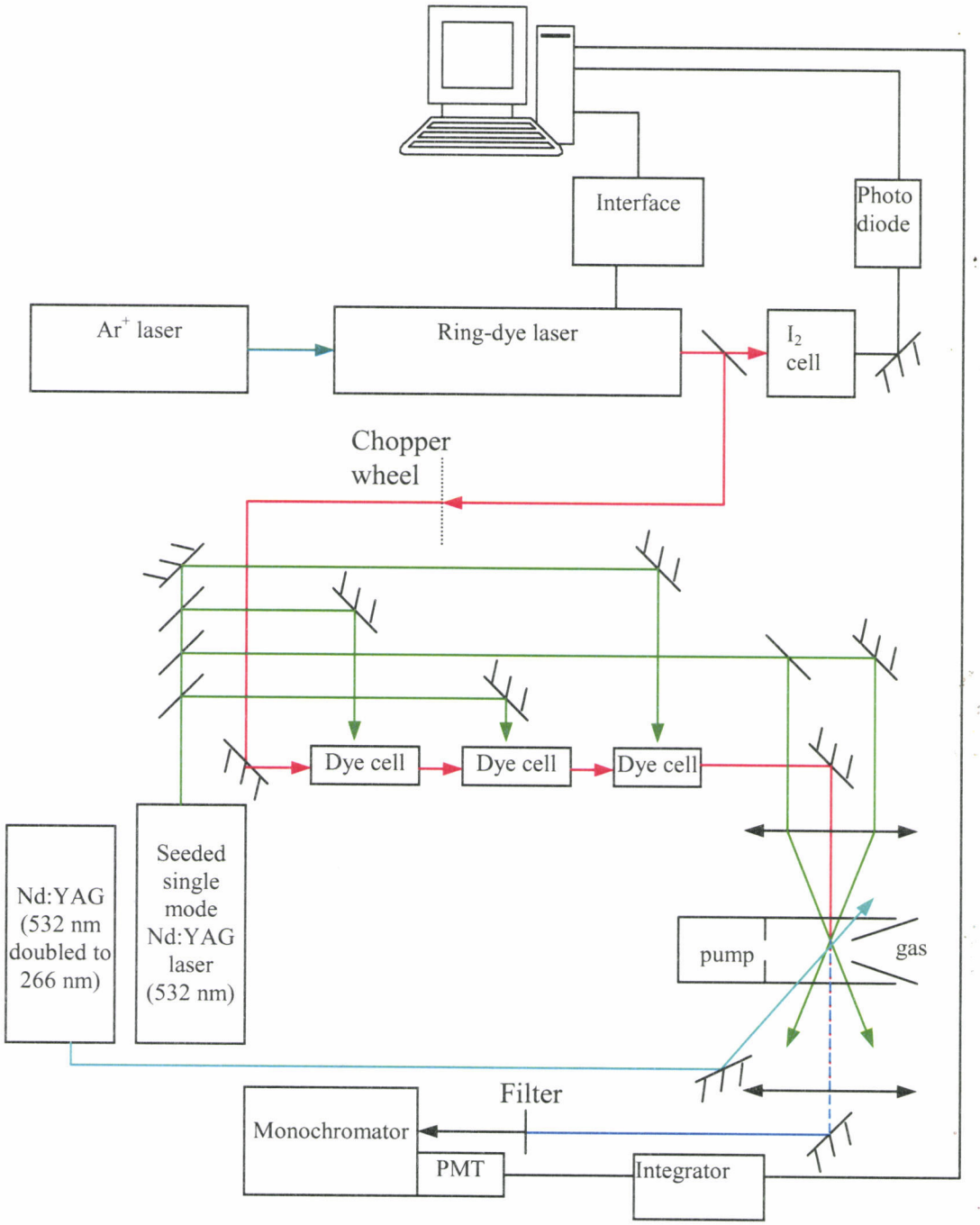

Figure 3-8 – CARS experimental set-up

The set-up includes:

1. A custom built laser providing a 50 ns FWHM duration beam at 20Hz with up to 200mJ of energy as 532 nm beam.
2. A ring-dye laser Coherent 699-29 as Stokes beam using R6G dye.
3. A cw Coherent Innova 200 Argon-ion laser to pump the ring dye laser.
4. A Spectra-Physics Quanta Ray GCR 170 laser producing 532 nm beam which is doubled with a KDP crystal to give a 266 nm UV beam.

The cw Stokes beam is passed through three amplifier stages pumped by a portion of the 50 ns 532 beam. The first and second stages of the amplification chain contained a dye mixture of 1.6×10^{-4} M of R610 and 1.0×10^{-4} M of R640; the third chain was 10 times more dilute.

For calibration, part of the cw Stokes beam was sent through an I_2 cell and the absorption spectrum was recorded. The 532 nm pump beam was fixed at the frequency 18788.4624 cm^{-1} (50% blue side of iodine line 1111).

The CD_3I sample (Aldrich 99.5% purity) was pulsed in a vacuum cell through a General Valve pulsed nozzle of 0.500 mm diameter and was synchronized with the photolysis and CARS beams. The sample was at 0.4 atm, and the various carrier gases (He, Ar, SF_6) used were at 2 atm. Unless specified, the photolysis beam and the probing beams were delayed 50 ns and were positioned 1 mm from the nozzle opening. In all cases, the UV beam was be positioned such that the intensity of CD_3I CARS signal was minimized, usually to less than 10% of the original value.

3.6 – EXPERIMENTAL RESULTS

Calibration Tests and Effect of Time Delay. As said in the previous section, the calibration of each recorded spectrum was done using the absorption spectrum of I_2. The frequencies of I_2 absorption lines are reported in the I_2 Atlas[37]. Spectra were then taken of CD_3 that were similar to the uncalibrated composite spectrum shown in Figure 3-2. An example is shown in Figure 3-9 below, where CD_3 product from photolysis of an expansion of neat CD_3I was examined at two delay intervals. No CD_3 was seen after 100 ns but from comparison of the 25 ns delay spectrum with the composite spectrum of Figure 3-1, we can calibrate the composite spectra to within an absolute wavenumber uncertainty of $\pm$ 0.01 cm^{-1}.

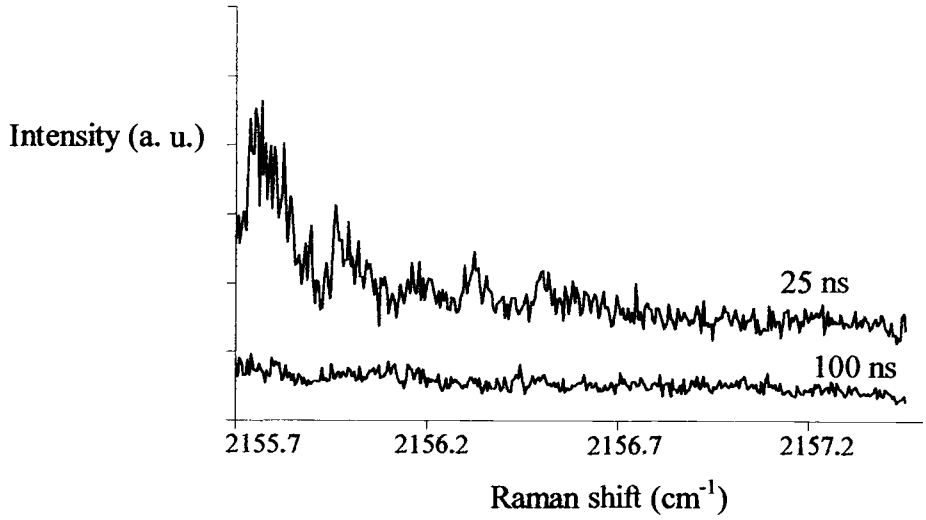

Figure 3-9 – Spectra of CD_3 at different delays

Jet Cooling of CD_3I Precursor. Calibrated spectra were also obtained for CD_3I at 295 K (static cell) and in a jet expansion of neat CD_3I where the temperature was estimated from modeling to be about 130 K (Figure 3-10). This cooling of the parent molecule in a jet is advantageous since our earlier studies of CH_3 showed that the spectra were simplified under some jet conditions that cooled the parent before photolysis. We also investigated the effect of driving the expansion by several gas carrier (He, Ar, SF_6) to see which might best cool the radical, so as to enhance low N, K features in the spectrum. The differences were minor and are illustrated by the spectra shown for Ar in Figure 3-10.

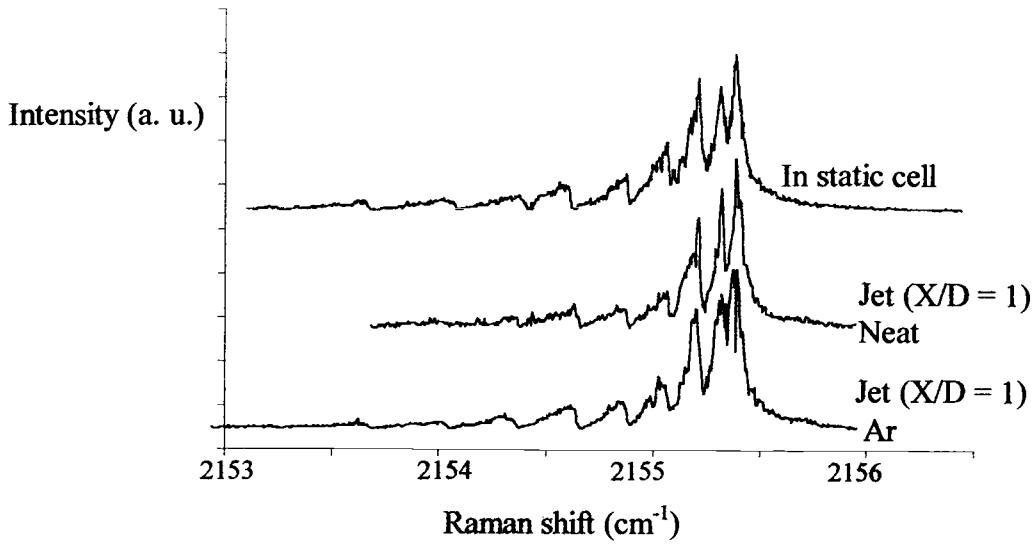

Figure 3-10 – Spectra of CD_3I in a static cell and in a jet with and without Ar driving gas

It should be noted that, unlike the case for CH_3I, where the CH_3 spectral features are well removed from those of the parent, the CD_3I Q-branches fall in the middle of the CD_3 spectral range. Since not all parent was photolyzed, this makes less certain the identification of all spectral features below about 2155 cm^{-1}. This overlap was not a problem in Miller's work where presumably the parent band for the CD_3NNCD_3 was apparently well removed from the CD_3 spectral region.

Effect of Collisions on the Spectra of CD_3. The earlier investigation of the radical CH_3 showed that the population of high N and K states differs significantly for spectra taken at various distances X from the nozzle[12]. These distances are expressed as X/D where D is the nozzle diameter. Figure 3-11 illustrates this and it is seen that at X/D = 8, only the low N, K states were populated, the CH_3 radical having on average only 3 collisions with a He atom.

Unfortunately, because the state density is about doubled for CD_3, the relative intensities of the spectral features are much reduced and it was not possible to obtain spectra at large X/D distances. Thus the peaks seen on the composite spectrum in Figure 3-2 are believed to correspond not to the beginning of the Q-branch (band origin) but to transitions of high N and K values, states populated due to the high number of collisions in the higher jet densities at small X/D values. In contrast, the low resolution measurements of Miller *et al.*[11] were made in a static cell with a time delay such that the sample was nearly thermalized at a temperature of 325K, conditions that favor low N, K transitions. Also, the kinetic energy in the

nascent dissociation steps following photolysis of azomethane-d_6 is low so thermal equilibrium is achieved after relatively few collisions. In contrast, in the case of CD_3I photolysis it is known that a much larger excess kinetic energy is given to the CD_3 fragment, so that the rapid collisional heating such as that seen for CH_3 in Figure 3-11 is reasonable.

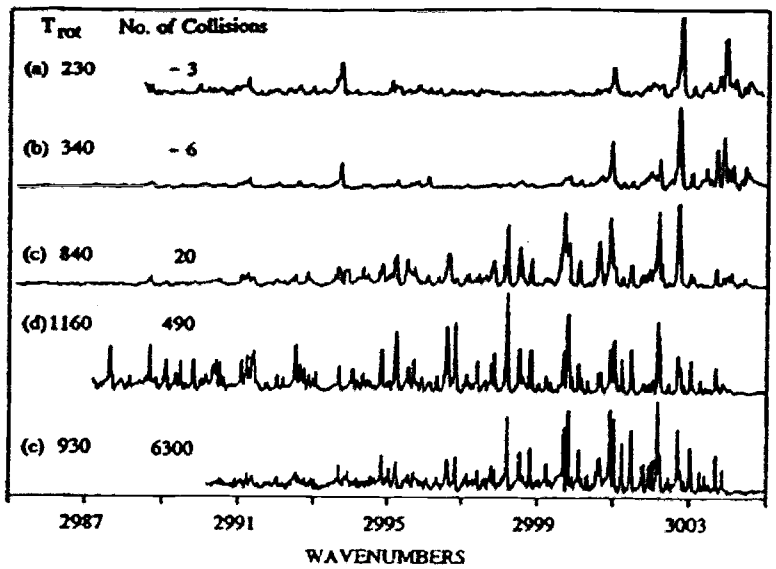

Figure 3-11 – CH_3 CARS spectra produced by photolysis of 0.46 atm CH_3I in 4 atm He jet at various jet positions. X/D=8, 5, 3, 0.3, and 0.5 for traces (a)-(e), respectively. For (a)-(d) the collision time between photolysis and probing was 20 ns; for (e) it was 370 ns.

Some efforts were made to try to absorb this excess kinetic energy via collisions with added driving gases such as He, Ar, SF_6. In the latter case, it was

hoped that the internal vibrational-rotational levels of SF_6 would act as a sink for the excess energy. This proved not to be helpful. The bottom trace in Figure 3-12 shows an expansion of neat CD_3I with no photolysis (a) and with photolysis (b, at greatly increased intensity). Also shown is the photolysis case when SF_6 was added (c, also at greatly increased intensity). The spectra show only slight hints of CD_3 features, with no indication that increased population in low N, K levels was occurring. For this reason, and because of limited amounts of CD_3I sample, it was concluded that no significant improvements in the composite CD_3 spectra of Figure 3-2 were likely so the remaining effort focused on the modeling of this, now calibrated, spectrum.

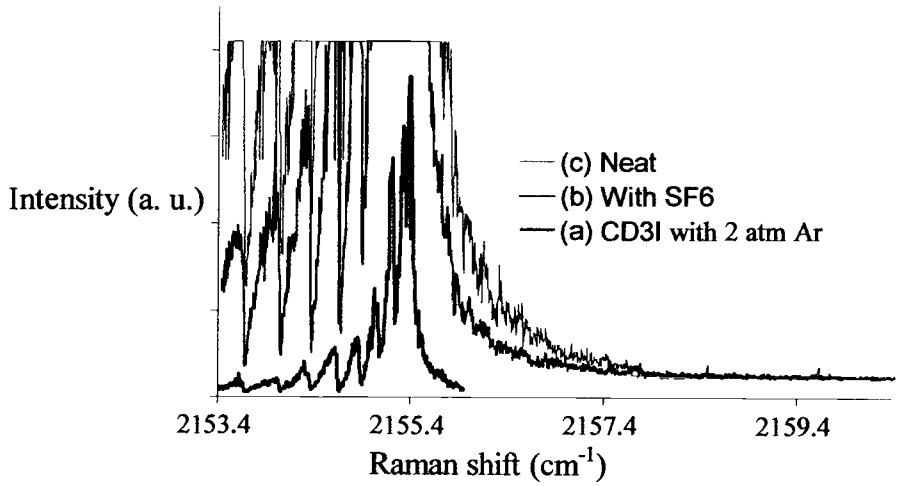

Figure 3-12 – Spectra at X/D = 1 of (a) CD_3I and CD_3 (b) with and (c) without SF_6

3-7 MODELING OF SPECTRA

CD_3 radical is an oblate symmetric top for which its rotational energy levels for each vibrational state is expressed as:

$$F_v(N,K) = BN(N+1) + (C-B)K^2 - D_N N^2(N+1)^2 - D_{NK}N(N+1)K^2 - D_K K^4 \qquad 3\text{-}3$$

where N is the quantum number characterizing the rotational angular momentum which couples with the unpaired electron spin to produce states of overall angular momentum characterized by J. K is the quantum number of the projection of this angular momentum along the molecular z-axis, B and C are the rotational constants and the D constants come from the centrifugal distortion.

The observed Q-branch (ΔN, $\Delta K = 0$) transitions were fit in the following expression:

$$\begin{aligned} Q(N, K) &= \nu_1 + F_1(N, K) - F_0(N, K) \\ &= \nu_1 + \Delta B\, N(N+1) + (\Delta C - \Delta B)\, K^2 \\ &\quad - \Delta D_N\, N^2(N+1)^2 - \Delta D_{NK}\, N(N+1)K^2 - \Delta D_K\, K^4 \qquad 3\text{-}4 \end{aligned}$$

Here $\Delta B = B_1 - B_0$ (= $-\alpha_B$, the vibration-rotation parameter), $\Delta C = C_1 - C_0 = -\alpha_C$, $\Delta D_N = D_{N1} - D_{N0}$, etc. The relative intensity of transition from the ground state N, K level is given by

$$n_{0NK} = (2N+1)\, g_{NK} \exp[-F_0(N, K)\, hc/kT] \qquad 3\text{-}5$$

where g_{NK} is the nuclear spin degeneracy factor explained in detail in the Appendix. It should be noted that this expression assumes a thermal equilibrium among the rotational levels that can be described by a Boltzmann distribution at

temperature T. In fact, thermal equilibrium is not likely and significant intensity variations can be expected, as has been observed for CH_3.

The starting point for the modeling was the ground state constants of Sears *et al.*[26] and the band origin and rotational constants of Miller *et al.*[11], as listed in Table 3-2. In the latter case, the usual planarity assumption $\Delta D_{JK} = -\frac{2}{3}(\Delta D_J + 2D_K)$ as well as the relation $D_K = D_J - 3B_v^3/2\omega_1^2$ derived from Silver and Shaffer[38] were made to reduce the number of fitting parameters.

	$\nu_1 = 2157.5$	Miller *et al.*	From CH_3 values
$B_0 = 4.80198$	$\Delta B = -\alpha_B =$	-0.026	-0.03147
$C_0 = 2.390$	$\Delta C = -\alpha_C =$	-0.018	-0.01667
$D_{N0} = 1.927\times10^{-4}$	$\Delta D_N =$	0.00001	0.000042
$D_{NK0} = -3.418\times10^{-4}$	$\Delta D_{NK} =$	-0.00002	-0.0000828
$D_{K0} = 1.600\times10^{-4}$	$\Delta D_K =$	0.00001	0.0000328

Table 3-2 – CD_3 constants used for a first fit (all values in cm^{-1})

Also shown in the table are initial estimates of CD_3 constants deduced from our CH_3 parameters[12] as follows. First, the ΔB and ΔC constants were assumed to

be reduced by the D/H isotopic mass ratio $(m_H/m_D)^{3/2}$ following the mass relation that has been derived for the rotational constants of diatomic molecules[39]. This, for example, predicts from ΔB for H_2 the value for D_2 to within 0.5%; a similar relation is expected for ΔB and ΔC for ν_1 of CH_3, CD_3 because the mass dependence is the same as for H_2, D_2. For ΔD's, a dependence of $(m_H/m_D)^2$ was assumed based on theoretical mass relations[39]. (The H_2 and D_2 comparison suggests that this may underestimate the mass dependence somewhat.) These initial estimates of CD_3 parameters from those of CH_3 are given in Table 3-2. The estimate of CD_3 band origin from the harmonic mass relation $(m_H/m_D)^{1/2}$ was not judged sufficiently reliable. This was also indicated by a force constant calculation (Appendix B), thus the ν_1 value reported by Miller *et al.* was used initially.

These values were then entered into a spreadsheet (CD3 fitting.xls) which calculated all transitions and Raman intensities assuming a Boltzmann distribution at a specified rotational temperature. These data were then processed by the CARS Specall program, which takes into account interference effects and linewidth convolutions, as described in reference 15. Part of the input here is a Lorentzian linewidth, which would eventually be adjusted to 0.03 cm^{-1} to match the observed linewidths in the composite spectrum.

Figure 3-13 displays a comparison between Miller's low resolution experimental spectrum and spectra calculated using his constants and those deduced from CH_3 values; both calculated spectra are for 325 K and both have the same band origin for reasonable comparison. They have also been convoluted with

a 0.15 cm^{-1} gaussian function to account for Miller's instrumental resolution. As seen, neither calculated spectrum reproduces exactly the experimental one, but Miller's constants do give a better overall representation.

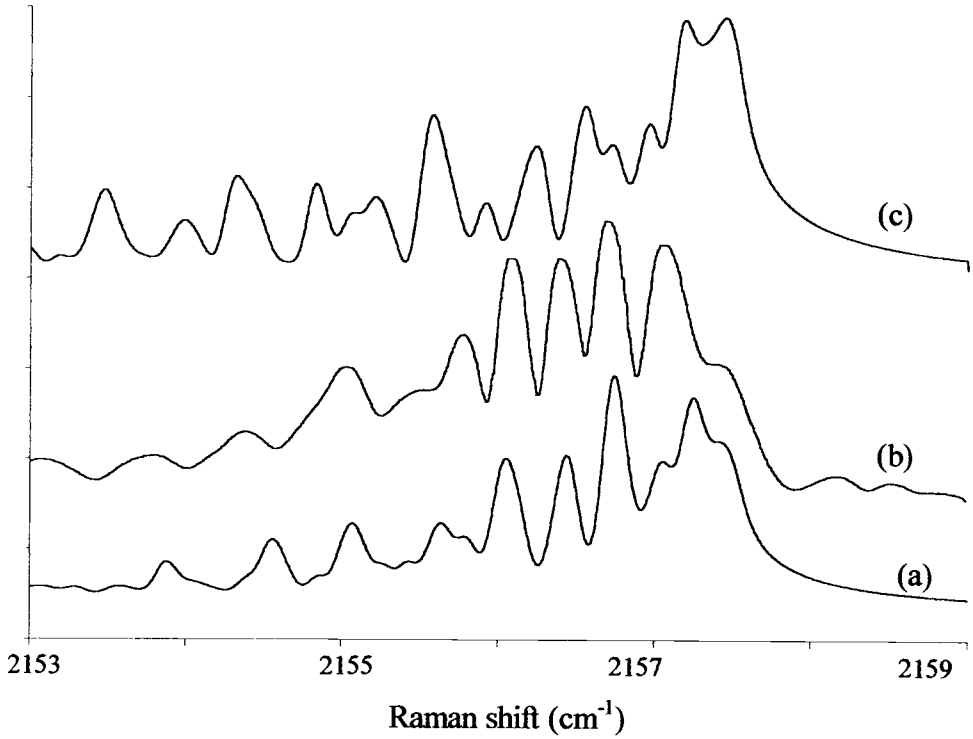

Figure 3-13 – Spectra (a) Obtained using Miller's constants; (b) Miller's experiment; (c) Obtained using values extrapolated from CH_3

We then used the same parameters to simulate spectra to compare with our higher resolution composite (Figure 3-14). A temperature of 800K was assumed based on approximate temperatures seen for CH_3 under comparable conditions.

Here, little correspondence is seen between either calculated spectrum and the experimental composite spectrum. In fact, this is expected since there is considerable uncertainty in both horizontal (wavenumber) and vertical (intensity) parts of the calculation. In particular, the intensities can be expected to show differences of perhaps as much as a factor of 10 from those predicted by a rotational Boltzmann distribution. The wavenumber display will be very sensitive to shifting by errors in the band origin estimate and to relative shifts in the peaks that result if the other rotational parameters for the band are varied. Finally, it must be remembered that residual features due to undissociated CD_3I confuse the region below 2156 cm^{-1} so that in seeking more optimal parameters, the region above this value has been emphasized.

The process for varying the parameters was as follows. First, we chose a rotational temperature of 800 K since that seemed to best describe the approximate relative intensities of CH_3 at the sampling point used for CD_3. We then systematically varied the four parameters ν_1, ΔB, ΔC, and ΔD_N (ΔD_{NK} and ΔD_K being determined by ΔD_N according to the relations mentioned earlier). Although tedious, this process allowed us to explore the reasonable "space" of these variables using predicted stick spectra like those shown at the bottom of Figure 3-15.

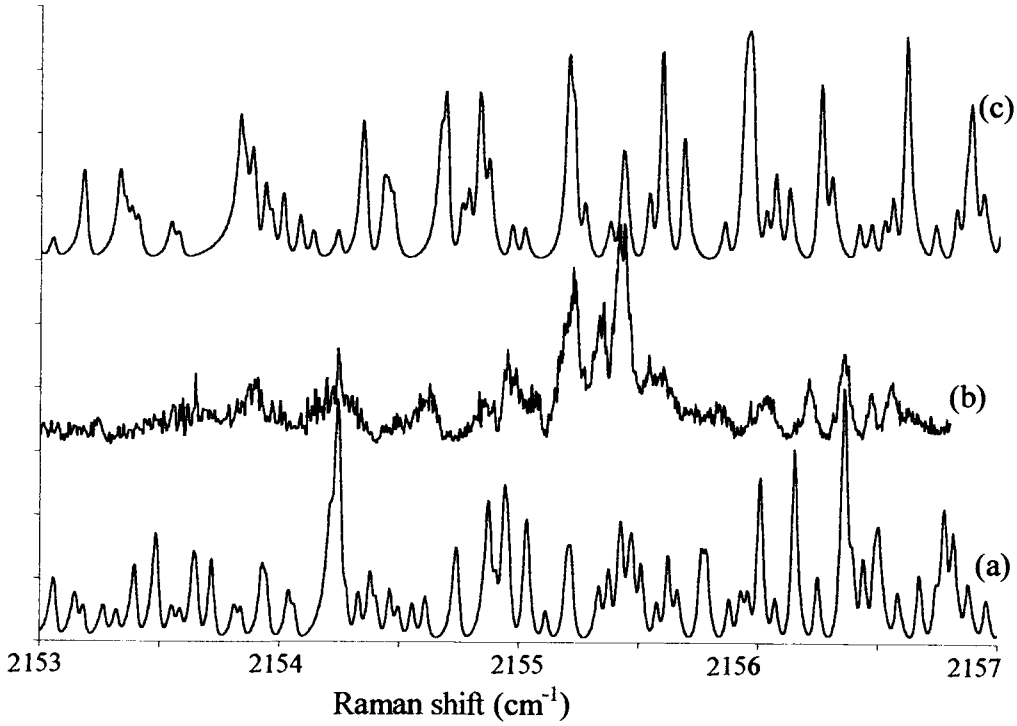

Figure 3-14 - (a) Spectrum obtained using Miller's parameters; (b) Composite experimental spectrum; (c) Spectrum obtained using parameters deduced from CH_3 values.

It was found that only a few choices for the assignment of the quartet of lines near 2156.5 cm^{-1} were acceptable. The maxima of these four peaks correspond to 2156.56, 2156.47, 2156.36 and 2156.21 cm^{-1}. On the next figures, only the region above 2155.5 cm^{-1} is displayed since only features in this region belong with certainty to the CD_3 radical.

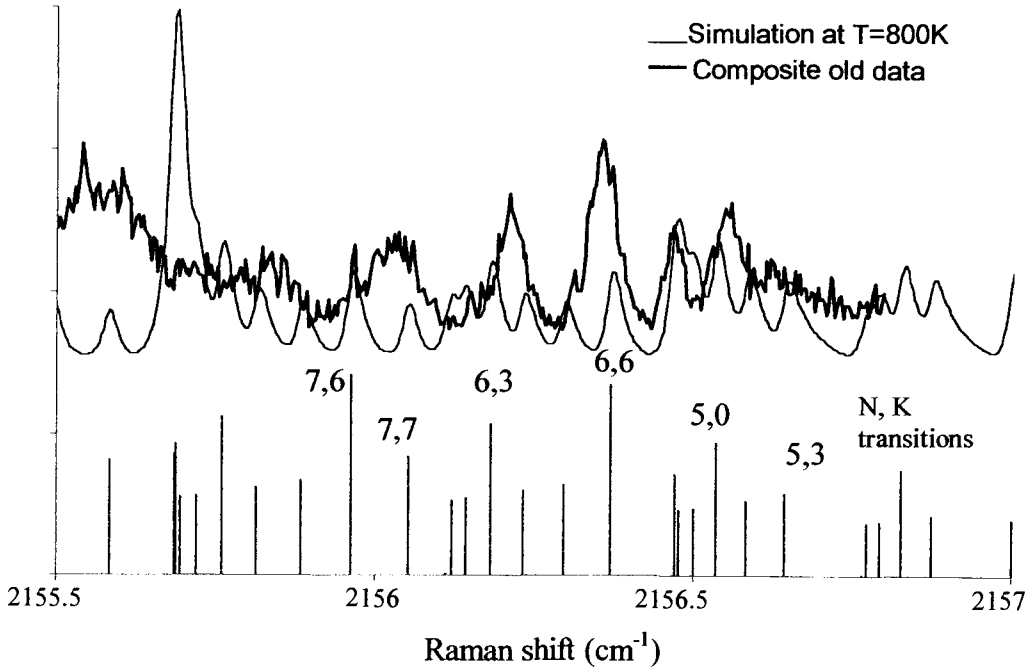

Figure 3-15 – Spectra of the composite and Case A fit as well as the N, K transitions

As examples of the modeling process, we consider two possible choices for the strong feature at 2156.35 cm^{-1}. In the first case (A), this feature was assigned as the N, K = 6,6 transition, which calculations indicated might be intense, and the parameters were varied to try to fit other members of the triplet. As seen in Figure 3-15, the spectral pattern obtained does not fit well the composite one, despite wide variations in the fitting parameters.

In the second case (B), the 2156.35 cm^{-1} peak was assigned as the N, K = 7,6 transition and the spectroscopic parameters were again varied. In this case a closer representation of some of the other transitions seemed to result; Figure 3-16

shows a comparison between our "best fit" spectrum (Case B) and the composite spectrum. The intensity match between the two spectra is of course far from perfect; in particular the simulated spectrum predicts an intense 9,9 transition feature around 2155.7 cm^{-1} and another around 2156.9 cm^{-1} for the 6,6 transition and neither is apparent in the observed spectrum. To some extent this may be due to the non-Boltzmann state populations that are expected in this dissociation although it is admittedly hard to understand how the population distribution could be so narrow as to exclude 6,6 and 9,9 populations while including some of the transitions displayed on this same figure that were used to fit the spectrum.

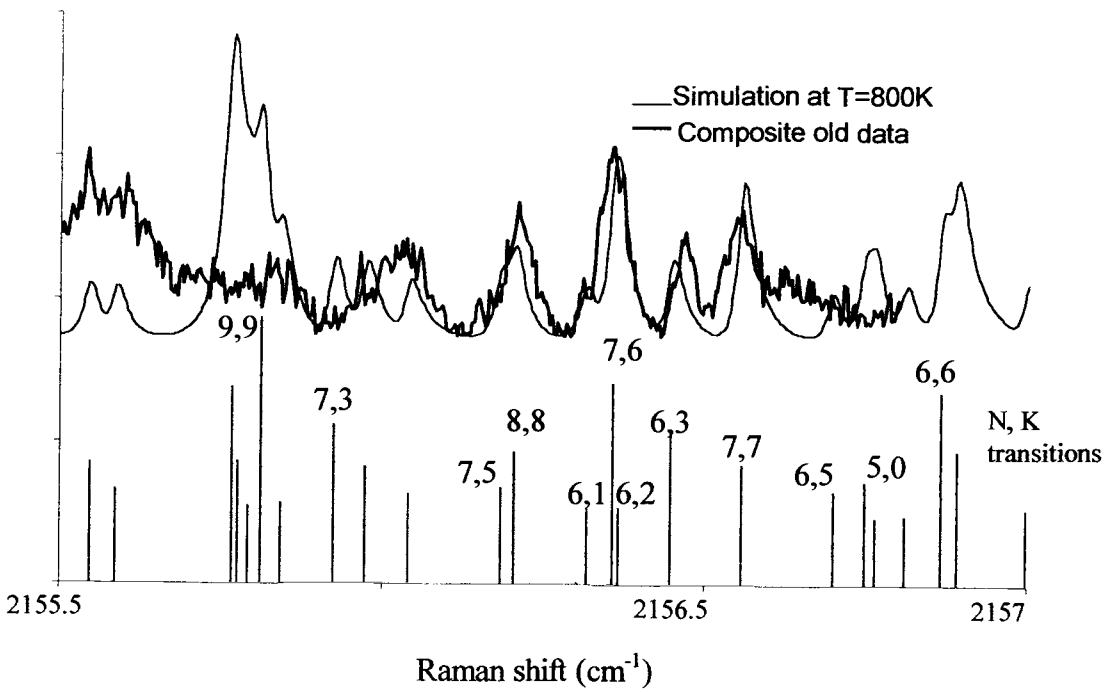

Figure 3-16 – Spectra of the composite and "best fit", and some of the N, K transitions

Despite this concern, we have used these assignments and the transition values reported in Table 3-3 to obtain the "optimal fit" of Figure 3-16 and the spectroscopic parameters given in Table 3-4. While the resultant values are quite reasonable, it must be said that the assignments and parameters can only be viewed as tentative at present.

N	K	Frequencies (cm^{-1})
7	7	2156.558869
6	3	2156.468807
7	6	2156.355395
6	2	2156.382081
6	1	2156.312032
8	8	2156.208627
7	5	2156.191949

Table 3-3 – Transitions used for Case B fitting.

2156.35 cm^{-1} is	Case A: 6,6	Case B: 7,6
ν_1	= 2157.3460 cm^{-1}	2157.8431 cm^{-1}
$\Delta B = -\alpha_B$	= -0.02870 cm^{-1}	-0.03598 cm^{-1}
$\Delta C = -\alpha_C$	= -0.02231 cm^{-1}	-0.02108 cm^{-1}
ΔD_N	= 0.000017 cm^{-1}	
ΔD_{NK}	= -0.000034 cm^{-1}	
ΔD_K	= 0.000017 cm^{-1}	

Table 3-4 – Constants used for Case A and Case B

3-8 CONCLUSION

A CARS experiment has been performed in a jet on the CD_3 radical produced by the photolysis of CD_3I. Features due to the ν_1 symmetric stretch were seen and carefully calibrated but the study was not as successful as hoped. Although the use of a jet does cool the sample, it was not possible to probe at high X/D values where simpler spectra are expected. This is because at these distances the intensities of the features are low due to a higher state density for CD_3 than CH_3. The study did reproduce data taken in earlier work and did yield calibrated transitions due to the parent molecule. This has allowed modeling of a composite

CD_3 spectrum, which is at much higher resolution that that obtained in an earlier study by Miller *et al.*[11]. This modeling leads to a tentative assignment of the CD_3 spectral features but this cannot be regarded as conclusive. The work indicates that some other probing method, such as double resonance Ionization-detected Stimulated Raman Spectroscopy, will probably be necessary to obtain more accurate information on the CD_3 radical species.

BIBLIOGRAPHY

1. C. V. Raman, K. S. Krishnan, *Nature*, **121** (1928) 501.

2. J. R. Ferraro, K. Nakamoto, *Introductory Raman Spectroscopy*, Academic Press (1994).

3. R. W. Boyd, *Nonlinear optics*, Academic Press, 1992.

4. A. B. Harvey, Anal. Chem. **50**, 905 (1978).

5. G. S. He, S. H. Liu, *Physics of Nonlinear Optics*, Chap 8, World Scientific, River Edge, NJ (1999).

6. C. A. Grant, J. L. Hardwick, *J. Chem. Ed.*, **74** (1997) 318.

7. IPCS, *Benzene,* World Health Organization, Geneva (1993).

8. James D. Ingle Jr, Stanley R. Crouch, *Spectrochemical Analysis*, Prentice Hall, New Jersey (1988).

9. G. Herzberg, *Molecular Spectra and Molecular Structure II: Infrared and Raman Spectra*, pp. 193, 362-369, reprint ed., Krieger, Melbourne, FL (1990).

10. E. B. Wilson, J. C. Decius, P. C. Cross, *Molecular Vibrations*, chap.10, McGraw Hill, New York (1955).

11. J. T. Miller, K. A. Burton, R. B. Weisman, W. Wu, P. S. Engel, Chem. Phys. Lett. **158** (1989) 179.

12. M. Zahedi, J. A. Harrison, J. W. Nibler, J. Chem. Phys. **100** (1994) 4043.

13. J. W. Nibler, G. V. Knighten, in: *Raman spectroscopy of gases and liquids*, ed. A. Weber (Springer, Berlin, 1979).

14. J. A. Shirley, R. J. Hall, A.C. Eckbreth, Opt. Letters **5** (1980) 380.

15. Engelene t. H. Chrysostom, PhD thesis, Oregon State University, 2001

16. J. Warnatz, U. Maas, R. W. Dibble, *Combustion*, Springer, 3rd edition (2001).

17. G. Herzberg, J. Shoosmith, Can. J. Phys, **34** (1956) 523.

18. A. D. Walsh, J. Chem. Soc, (1953) 2296.

19. G. Herzberg, Proc. Roy. Soc. A **262** (1961) 291.

20. P. Botschwina, J. Flesch, W. Meyer, Chem. Phys. **74** (1983) 321.

21. D. E. Milligan, M. E. Jacox, J. Chem. Phys. **47** (1967) 5146.

22. A. Snelson, J. Phys. Chem. **74** (1970) 537.

23. V. Spirko, P. R. Bunker, J. Mol. Spec, **95** (1982) 381.

24. C. Yamada, E. Hirota, K. Kawaguchi, J. Chem. Phys, **75** (1981) 5256.

25. G. N. A. Van Veen, T. Baller, A. E. De Vries, N. J. A. Van Veen, Chem. Phys, **87** (1984) 405.

26. J. M. Frye, T. J. Sears, D Leitner, J. Chem. Phys, **88** (1988) 5300.

27. G. E. Hall, T. J. Sears, J. M. Frye, J. Chem. Phys, **90** (1989) 6234.

28. D. H. Parker, Z. W. Wang, M. H. M. Janssen, D. W. Chandler, J. Chem. Phys, **90** (1989) 60.

29. T. Amano, P. F. Bernath, C. Yamada, Y. Endo, E. Hirota, J. Chem. Phys. **77** (1982) 5284.

30. W. M. Fawzy, T. J. Sears, J. Chem. Phys, **92** (1990) 7021.

31. R. N. Rudolph, G. E. Hall, T. J. Sears, J. Chem. Phys, **105** (1996) 7889.

32. J. W. Hudgens, T. G. DiGiuseppe, M. C. Lin, J. Chem. Phys. **79** (1983) 571.

33. I. Powis, J. F. Black, J. Chem. Phys, **93** (1989) 2461.

34. S. G. Westre, P. B. Kelly, J. Chem. Phys, **90** (1989) 6977.

35. M. L. Orlov, J. F. Ogilvie, J. W. Nibler, J. Mol. Spec. **185** (1997) 128.

36. H. C. Allen, P. C. Cross, *Molecular Vib-rotors*, John Wiley & Sons (1963).

37. S. Gertenkorn , P. Luc, Atlas du spectre d'absorption de la molécule d'iode (CNRS, Paris, 1978).

38. S. Silver, W. H. Shaffer, J. Chem. Phys. **9** (1941) 599.

39. I. N. Levine, *Molecular Spectroscopy*, Wiley Interscience (1975) p155.

APPENDICES

APPENDIX A

CALCULATION OF THE STATISTICAL WEIGHTS FOR CD_3

The total wavefunction ψ_T of a molecule is usually expressed as:

$$\psi_T = \psi_e \psi_s \psi_r \psi_v \qquad \text{A-1}$$

where ψ_e is the electronic wavefunction, ψ_s the spin wavefunction, ψ_r the rotational wavefunction, and ψ_v the vibrational wavefunction. Deuterium is a boson since its nuclear spin I is 1. Thus the total wavefunction has to be symmetric to exchange of identical nuclei. The ground electronic state CD_3 is known to be a_2''[19]. The mode of vibration studied in this case is ν_1, so ψ_v is symmetric (a_1' symmetry). This leaves us the symmetries of ψ_s and ψ_r to be investigated.

For the ψ_r case, we only need to consider the rotational subgroup of CD_3. CD_3 belongs to the D_{3h} group; hence, its subgroup will be D_3 which character table is given in Table A-1.

D_3	E	$2C_3$	$3C_2$
A_1	1	1	1
A_2	1	1	-1
E	2	-1	0

Table A-1 – D_3 Character table

The rotational wavefunction for a symmetric rotor is expressed as

$$\psi_{NKM}(\theta, \phi, \chi) = \Theta(\theta)\, e^{iK\chi}\, e^{iM\phi} \qquad \text{A-2}$$

where N is the rotational angular momentum quantum number, K is the quantum number of the projection of this angular momentum along the molecular z-axis, and M is the quantum number of the projection of the angular momentum along the laboratory Z-axis. $\Theta(\theta)$ is a hypergeometric function of $\sin^2(\theta/2)$. θ, χ and ϕ are the Eulerian angles defining the orientation of the molecular system relative to the laboratory system (Figure A-1).

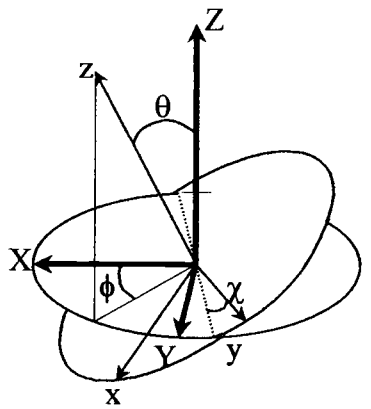

Figure A – Euler angles θ, ϕ, χ relating the molecular system (x, y, z) to the laboratory system (X, Y, Z)

We now consider the effects of the symmetry operations of the rotational wavefunction. Under the identity operation E, the rotation wavefunction remains unchanged:

$$\psi_{NKM}(\theta, \phi, \chi) \xrightarrow{E} \psi_{NKM}(\theta, \phi, \chi)$$

So, for $K = 0$, $\chi'_E = 1$, and for $|K| \neq 0$, $\chi'_E = 2$ since the levels are doubly degenerate.

Under the three-fold rotation operation, C_3, the Eulerian angle χ becomes $\chi + \frac{2\pi}{3}$. So the transformation is:

$$\psi_{NKM}(\theta, \phi, \chi) \xrightarrow{C_3} \psi_{NKM}(\theta, \phi, \chi+2\pi/3) = e^{i2\pi K/3}\, \psi_{NKM}(\theta, \phi, \chi)$$

For $K = 0$, the wavefunction is unchanged, thus $\chi'_{C_3} = 1$. If $|K| \neq 0$, for any N and M, there are two wavefunctions, ψ_{NKM} and ψ_{N-KM}, and the character of this operation will then be:

$$\chi'_{C_3} = e^{\frac{i2\pi K}{3}} + e^{\frac{-i2\pi K}{3}} = 2\cos\left(\frac{2\pi K}{3}\right) \qquad \text{A-3}$$

So, for $|K| = 3p$ (with p = 1, 2, 3...) $\chi'_{C_3} = 2$, but for $|K| = 3p \pm 1$, $\chi'_{C_3} = -1$.

The final operation C_2 is a two-fold rotation about an axis perpendicular to the symmetry axis. This axis makes an angle α with the x-axis. The change in the wavefunction will then be:

$$\psi_{NKM}(\theta, \phi, \chi) \xrightarrow{C_2} \psi_{NKM}(\pi-\theta, \pi-\phi, \pi-\chi+2\alpha) = (-1)^{N+n+M} e^{iK(\pi+2\alpha)}\psi_{NKM}(\theta, \phi, \chi)$$

where n is the larger of $|K|$ and $|M|$. Therefore, if N is odd $\chi'_{C_2} = -1$, and N even $\chi'_{C_2} = 1$. If these results are regrouped in a table, it is then easy to assign the symmetry of each rotation level (Table A-2).

Energy levels	χ'_E	χ'_{C_3}	χ'_{C_2}	Symmetry
$K = 0, N$ even	1	1	1	A_1
$K = 0, N$ odd	1	1	-1	A_2
$\lvert K \rvert = 3p$	2	2	0	$A_1 + A_2$
$\lvert K \rvert = 3p \pm 1$	2	-1	0	E

Table A-2 – Characters for the representation of D_3 formed by ψ_{NKM} (with p = 1, 2, 3...)

Finally, we consider the spin wavefunction ψ_s. Since the nuclear spin of the deuterium is I = 1, there are $(2I + 1)^3 = 27$ spin states. Because of the value of the nuclear spin, the spin can either be 1, 0 or –1. If a table were made with a combination of these values for each deuterium atom (called D_a, D_b, D_c) we should obtain 27 combinations (Table A-3).

D_a	D_b	D_c
1	1	1
1	1	0
1	0	1
1	0	0
1	0	-1
1	-1	0
1	-1	-1
1	-1	1
1	1	-1

Table A-3 – 9 out of the 27 different combinations

Under the identity operation, none of the combinations are changed so the reducible character is $\chi'_E = 27$. When a three-fold rotation occurs, D_b becomes D_a, D_c becomes D_b, and D_a becomes D_c. Among the 27 combinations, only the three (1,1,1), (0,0,0), (-1,-1,-1) remain unchanged so $\chi'_{C_3} = 3$. A two-fold rotation occurs about an axis perpendicular to the symmetry axis. This axis could be the C—D_c bond. Then D_b becomes D_a and vice-versa. Among the 27 combinations, only 9 remain unchanged. So $\chi'_{C_2} = 9$. It is then easy to reduce this reducible representation to show that the 27 ψ_s wavefunctions have $10A_1+A_2+8E$ symmetry.

Having the symmetry of each wavefunction, the statistical weights of the vibrational-rotational levels can be deduced[36] using the direct product table of D_3

(Table A-4). The results are grouped in Table A-5 and are used in modeling the CARS spectra obtained in this thesis work.

D_3	A_1	A_2	E
A_1	A_1	A_2	E
A_2		A_1	E
E			A_1+A_2+E

Table A-4 – Direct product table of D_3

ψ_e	ψ_s	ψ_v	ψ_r		weights of ψ_T
			A_1	for $K = 0$ N even	1
A_2	$10A_1+A_2+8E$	A_1	A_2	for $K = 0$ N odd	10
			$A_1 + A_2$	for $\lvert K \rvert = 3p$	11
			E	for $\lvert K \rvert = 3p \pm 1$	8

Table A-5 – Statistical weights of vibrational-rotational levels.

APPENDIX B

CALCULATION OF THE CD_3 FORCE CONSTANTS

This calculation was performed using the program Asym40.exe. Part of its input involved the coordinate and the mass of each atom, for each isotopomer CH_3, CH_2D, CHD_2 and CD_3. The CH_3 and CD_3 vibrational frequencies of Table 3-1 were entered with equal uncertainties chosen somewhat arbitrarily. The program gave results for the force constants, as well as the calculated values of the different vibrational frequencies for each isotope. These latter results are reported in Table A-6. The C-H stretch force constant is found out to be 520.4 N/m and the force constant describing the interaction between the bonds 10.5 N/m. The CH force constant is known to increase as the C hybridized orbitals have increasing s orbital character. For example, from Table 2-4, the force constant for the $C(sp^3)$-H stretch is 479 N/m and for the $C(sp^2)$-H stretch is 510 N/m. The radical force constant is thus in agreement with these predictions since the carbon atom in the radical is the prototype of sp^2 hybridization.

	CH_3			CD_3		
	Observed (cm^{-1})	Calculated (cm^{-1})	Difference (cm^{-1})	Observed (cm^{-1})	Calculated (cm^{-1})	Difference (cm^{-1})
ν_1	3004.420	3019.619	-15.199	2157.5	2136.014	21.486
ν_2	606.453	600.493	5.960	457.813	465.501	-7.688
ν_3	3160.821	3163.320	-2.498	2391.089	2387.779	3.310
ν_4	1396.000	1401.639	-5.638	1026.000	1018.238	7.762

Table B-1 – Observed and calculated vibrational frequencies for CH_3 and CD_3 using Asym40.exe program